Research Article Vol. 34, No. 5 / 9 Mar 2026 / Optics Express 7388
Optics EXPRESS

Dual-modal all-fiber OCT needle probe integrated with FBG for simultaneous imaging and temperature sensing

MINGHUI CHEN,[1] RUI BAO,[1] HAOCHEN HU,[1] ZIXUAN YIN,[1] ZIYI HUANG,[2,3] CHENYANG SU,[2,3] ZESEN ZHANG,[2,3] JIANAN LI,[4] YIPING WANG,[2,3] DEJUN LIU,[2,3,5] AND CHANGRUI LIAO[2,3,6]

[1]*Shanghai Engineering Research Center of Interventional Medical Device, the Ministry of Education of Medical Optical Engineering Center, School of Health Sciences and Engineering, University of Shanghai for Science and Technology, Shanghai 200093, China*
[2]*Key Laboratory of Optoelectronic Devices and Systems of Ministry of Education and Guangdong Province, College of Physics and Optoelectronic Engineering, Shenzhen University, Shenzhen, China*
[3]*Shenzhen Key Laboratory of Ultrafast Laser Micro/Nano Manufacturing, Guangdong and Hong Kong Joint Research Centre for Optical Fiber Sensors, State Key Laboratory of Radio Frequency Heterogeneous Integration, Shenzhen University, Shenzhen 518060, China*
[4]*Xi'an Institute of Optics and Precision Mechanics, Chinese Academy of Sciences, Xi'an 710119, China*
[5]*dejun.liu@szu.edu.cn*
[6]*cliao@szu.edu.cn*

Abstract: We designed and fabricated a single-fiber needle probe integrated with a fiber Bragg grating (FBG) capable of simultaneously performing optical coherence tomography (OCT) imaging and temperature sensing. The Bragg wavelength of the FBG is designed to fall within the spectral bandwidth of the OCT light source, enabling dual-mode functionality with a single OCT source. The probe exhibits a lateral resolution of approximately 30 μm, operates at a working distance of about 0.9 mm in air, and features a temperature sensitivity of 10.14 pm/°C. Grating reflectance has a significant influence on OCT imaging performance; hence, multiple fiber probes with varying grating parameters were investigated. Results indicate that limiting grating reflectance to ≤24% serves as a reference threshold for balancing high-quality imaging with precise temperature sensing. Finally, experiments conducted on ex vivo mouse brains and porcine backfat further demonstrate the potential applications of this dual modal OCT needle probe.

1. Introduction

Optical coherence tomography (OCT), as a high-resolution, high-speed, and highly sensitive optical imaging technique, has emerged as one of the most promising tomographic imaging technologies developed in decades [1]. A key direction for advancing OCT is the development of miniaturized all-fiber probes, which have garnered significant attention due to their microstructure, allowing them to enter narrow human structures such as blood vessels [2–5] and pancreaticobiliary ducts [6] for imaging diagnostics. Current advancements in OCT imaging are pursuing two primary paths: one aims to enhance performance metrics such as resolution [7–10] and depth of focus (DOF) [11–13], while the other seeks to broaden its applications through integration with complementary technologies, including another imaging technique, such as photoacoustic imaging, and non-imaging techniques such as sensors that can acquire other physical/chemical information.

Currently, double-clad fibers are commonly used to achieve effective coupling between OCT imaging and sensors [14,15]. Fluorescence-based sensing combined with OCT has become

#586141 https://doi.org/10.1364/OE.586141
Journal © 2026 Received 28 Nov 2025; revised 4 Feb 2026; accepted 5 Feb 2026; published 23 Feb 2026

Optics EXPRESS

a popular method for simultaneously acquiring OCT structural images and sensing functional parameters. The use of double-clad fibers enables efficient coupling of fluorescence signals with OCT signals, integrating fluorescence imaging and OCT within a single fiber probe [16]. The specific tissue labeling of fluorescent molecules combined with OCT's high-resolution imaging allows simultaneous diagnostic imaging of target locations. Furthermore, fluorescent molecules sensitive to pH [17], temperature [18], and other specific parameters can be employed for sensing. A polymer coating doped with these specific fluorescent molecules can be deposited onto the tip of the fiber probe [19], and pH or temperature values can be recorded by monitoring the emission spectrum of this dye. Alternatively, fluorescent molecules can be used to label the tissue being tested directly. However, when excitation light is incident on tissue samples, the tissue itself generates background autofluorescence [20], which affects the detection of fluorescence intensity, thereby impacting the accuracy of target information (temperature, pH, etc.). In comparison, rare earth ion temperature measurement offers greater advantages. Fusing glass containing rare-earth ions into OCT imaging fibers based on double-clad fibers enables temperature measurement through changes in the intensity of the upconversion fluorescence spectrum emitted by Er^{3+}/Yb^{3+} rare-earth ions [21]. This approach avoids the influence of tissue autofluorescence. However, the 980 nm excitation light falls within the strong absorption band of water molecules, resulting in significant laser-induced heating effects. This non-specific heating not only alters the true temperature of the sample, severely compromising the accuracy of temperature sensing, but may also cause damage to living tissue [22]. Obviously, the incorporation of additional laser sources typically results in extra and undesirable tissue effects. It should be noted that the use of double-clad fibers inevitably generates artifacts in OCT imaging [23], which can affect the accuracy of the imaging information. This effect is a direct consequence of the underlying architecture of double-clad fibers.

This paper proposes an OCT-FBG single-fiber needle probe that simultaneously achieves OCT imaging and temperature sensing within tissue using an OCT light source, which features a simple structure, is lightweight, and slim. Fiber Bragg grating (FBG) is an optical sensor exhibiting a linear relationship between reflected wavelength and temperature [24], providing real-time, high-precision (10.14 pm/°C) temperature feedback. The needle probe developed in this study performs both functions using only an OCT light source. This approach minimizes interference from additional lasers while reducing system complexity and cost. By selecting gratings with appropriate parameters, the probe can perform both imaging and temperature measurement functions, while the impact on OCT imaging remains controllable. This dual-function needle probe enables diagnostic puncture into deep tissues, holding considerable potential for clinical translation. For instance, this needle probe shows potential for cancer tissue diagnosis. They provide OCT images and sense higher temperatures in cancerous tissues, which result from increased cellular metabolism and dense vascularization [25]. This combined data offers multi-parameter support for the in vivo localization of malignant tumors. To validate the feasibility of our dual-function probe, we conducted real-time temperature measurement and OCT imaging experiments on ex vivo mouse brains and porcine backfat.

2. Design and fabrication

2.1. Probe design and realization

Figure 1 shows the schematic structure of this all-fiber FBG-OCT probe. A ~1.6 m long single-mode fiber (SMF-28e, Thorlabs) was fusion-spliced with a graded-index (GRIN) fiber (GI 100/125-14/250, YOFC) using a fiber fusion splicer. Under a microscope, the fusion interface between the two fibers was localized, and a Bragg grating with a selected wavelength and length was then written point-by-point into the core of the single-mode fiber using a femtosecond laser. Grating length and laser power are shown in Table 1. For the single-mode fiber used, the effective index is ~1.447. Given our target Bragg wavelengths of 1310 nm and 1350 nm,

Optics EXPRESS

the corresponding design grating periods are approximately 452 nm and 466 nm, respectively. Writing the grating in proximity to the GRIN fiber (Fig. 1(b)) maximizes alignment between the probe's imaging position and the grating's temperature measurement location; the GRIN fiber length is sufficiently short (<1 mm). The GRIN fiber was cut to the desired length (820 μm) under microscopic conditions using a large-core fiber cutter (CT-105/s106, Fujikura, Japan). This FBG-OCT probe is an all-fiber design. For tissue imaging and temperature measurement, a 25G metal needle tip (outer diameter: 0.51 mm; inner diameter: 0.26 mm) can be selected as the protective sheath.

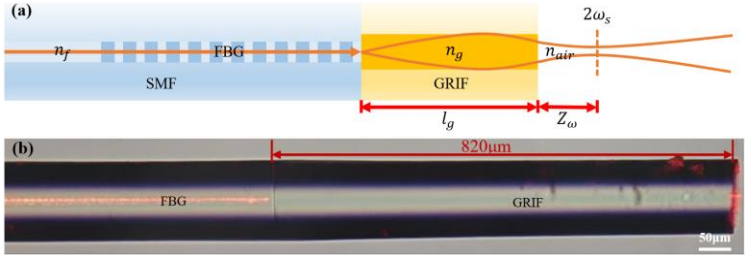

Fig. 1. A forward-viewing FBG-OCT single-fiber probe: (a) Schematic diagram of the probe's overall structure (SMF: single-mode fiber; GRIF: graded-index fiber); (b) Forward-viewing probe with a red-light source attached, showing the Bragg grating visible when the red-light source is connected.

Table 1. Bragg Grating Parameter

Probe	Length(mm)	Laser Power	Bragg wavelength(nm)	Reflectivity
1	2	25%	1306.1	96%
2	1	25%	1306.1	66%
3	0.5	25%	1305.8	28%
4	1.25	18%	1305.9	24%
5	1.25	18%	1345.9	24%
6	0.89	18%	1346.1	9%
7	0.59	18%	1346.2	5%
8	0.5	10%	1346.0	<5%
9 (without FBG)	/	/	/	/

The output beam of this probe can be characterized by the ABCD matrix, with its working distance (Z_w) and beam waist radius (w_s) expressed as [26]:

$$Z_w = \frac{n_{air}\left(1 - \left(\frac{a_0}{n_g g}\right)^2\right)\sin(2gl_g)}{2n_g g\left[\sin^2(gl_g) + \left(\frac{a_0}{n_f n_g g}\right)^2 (n_f \cos(gl_g))^2\right]} \tag{1}$$

$$w_s = \frac{a_0 w_0}{n_g g\sqrt{\sin^2(gl_g) + (\frac{a_0}{n_f n_g g})^2 (n_f \cos(gl_g))^2}} \tag{2}$$

Here, n_f, n_g, n_{air} are the refractive indices of the single-mode fiber core, the graded-index fiber core, and air, respectively. l_g is the length of the graded−index fiber, respectively, while

Optics EXPRESS

w_0 is the diameter of the single-mode fiber core. Furthermore, $a_0 = \frac{\lambda}{\pi {w_0}^2}$ and $z_R = \frac{\pi {w_s}^2}{\lambda}$. z_R is the Rayleigh length. Using a three-dimensional refractive-index tester (SHR-1602), the core refractive index of this GRIN fiber was measured as 1.46497, and the cladding refractive index as 1.45782. Based on the gradient refractive index formula $n(r) = n_g\ (1 - g^2r^2/2)$ [27], the gradient constant g of this fiber was calculated to be approximately 1.976 mm^{-1}. GRIN fibers with different lengths exert varying effects on beam focusing performance, influencing parameters such as the exit beam spot size and working distance. When the length of the GRIN fiber is 1/4 of the pitch ($P = 2\pi/g = 3.18$ mm), the beam can exit in a nearly collimated state. At this point, the Rayleigh length can reach a maximum of 2.96 mm, with a beam waist radius of 35.1 μm; the corresponding length of the GRIN fiber is 795 μm. When the fiber length is selected as 820 μm, the imaging depth (defined as the sum of the working distance and Rayleigh length) reaches a maximum of 3.55 mm, with a beam waist radius of 32.3 μm. So, the GRIN fiber length was ultimately determined to be 820 μm in the experiment, as it resulted in a smaller spot size and greater imaging depth. The corresponding working distance is 1.05 mm.

To quantitatively characterize the actual output beam quality of the fabricated fiber probes, this study systematically measured their spot characteristics using a beam quality analyzer (S-WCD-LCM-C-1310, Dataray). Figure 2 shows the variation curves of the spot diameter and full width at half maximum (FWHM) along the optical axis propagation distance for one of the fiber probes, and compares these results with simulations based on the ABCD matrix theory. Since the end face of the fabricated probe was only cut by a cutting tool without polishing, the probe end face is non-flat. This results in a smaller full width at half maximum (FWHM) of the light spot while causing beam divergence, thereby reducing the imaging depth. The average lateral resolution of the probes used in this study was approximately 30 μm, with a working distance of about 0.9 mm in air, and an imaging depth of ~ 2.4 mm.

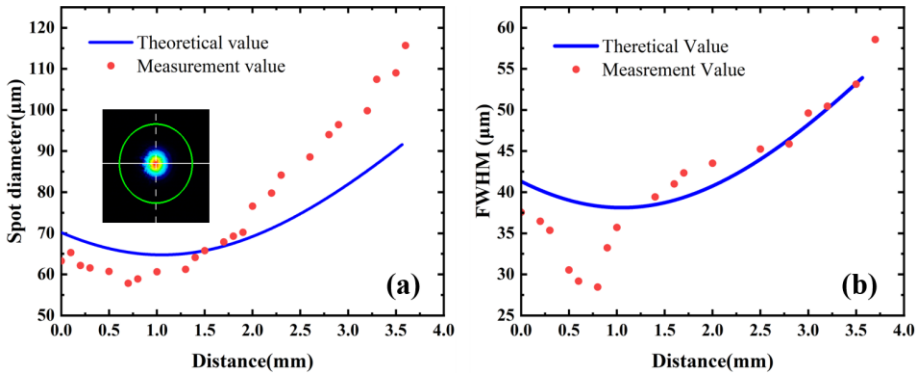

Fig. 2. (a) Spot diameter and (b) FWHM variation curves measured at various distances from the probe tip. An inset in (a) shows the spot image at the focus position.

2.2. *Working principle and characterization of FBGs*

As shown in Fig. 3, the grating engraved on the fiber probe reflects the incident OCT light at a specific wavelength, while allowing the majority of the light to transmit into the sample for imaging. In an optical fiber grating, light conforming to the Bragg condition is strongly reflected, while light at other wavelengths is transmitted. The Bragg reflection condition can be expressed by the following formula [28]:

$$\lambda_B = 2n_{eff}\Lambda \tag{3}$$

Among these, λ_B is the Bragg wavelength, n_{eff} is the effective refractive index of the fiber, and Λ is the period of grating. Generally, the spectral shift of FBGs is predominantly governed

Optics EXPRESS

by two factors: stress and temperature. Under mechanical stress, the shift is primarily caused by the elastic deformation of the grating period, which elongates under tension and contracts under compression. The accompanying change in refractive index from the photoblastic effect is typically negligible. Similarly, temperature changes induce a shift through the combined action of the thermo-optic effect, which alters the refractive index, and thermal expansion, which changes the grating period, with the thermo-optic effect being the dominant contributor. The formula for the corresponding Bragg wavelength drift is as follows [29]:

$$\Delta\lambda_B = (K_\varepsilon \Delta\varepsilon)\lambda_B + (K_T \Delta T)\lambda_B \tag{4}$$

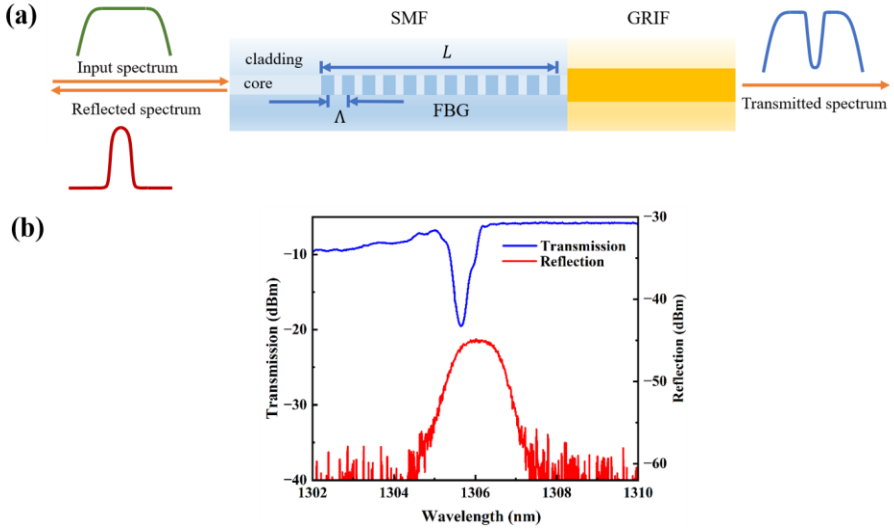

Fig. 3. Working principle of a fiber Bragg grating: in a schematic of the device, Λ is the grating period, and L is the grating length. (b) Reflected spectrum and transmitted spectrum.

In the equation, K_T and K_ε are the wavelength sensitivity coefficients of the fiber Bragg grating to temperature and strain. To ensure the accuracy of temperature measurements by the grating, the entire probe is encapsulated within a metal tip to prevent bending of the grating and the resulting strain. Consequently, the grating can be considered unaffected by external strain and suitable for temperature measurement.

For fiber Bragg gratings, when stress effects are neglected, the relationship between temperature and Bragg wavelength is expressed by the formula:

$$\Delta\lambda_B = \lambda_B(\xi + \alpha)\Delta T \tag{5}$$

That is, $K_T = (\alpha+\xi)$, where α is the thermal expansion coefficient of glass and ξ is the thermal optical coefficient, with values of $5.5 \times 10^{-7}°C^{-1}$ and $7 \times 10^{-6}°C^{-1}$ [28]. This indicates that the temperature exhibits a linear relationship with the center wavelength of the grating reflection spectrum, enabling temperature measurement based on this principle.

3. Experiments

3.1. OCT-FBG system

As shown in Fig. 4, this multi-modal system integrates OCT for imaging with an FBG interrogation system for sensing. Within the OCT imaging system, a swept-source laser (SVM131-2101, Thorlabs) is utilized, with a 100-kHz A-scanning frequency, a central wavelength of 1300 nm,

Optics EXPRESS

and a 100-nm continuous tuning range without mode jumps. Ignoring system effects, the axial resolution of OCT images produced by this light source is theoretically ~7.4 μm. In the OCT imaging subsystem, light emitted from the source is split by a coupler, where 10% of the light is directed into the reference arm and 90% into the sample arm. The light entering the reference arm is reflected, then coupled with the backscattered light from the sample via a circulator to generate an interference signal. A balanced photodetector detects the interference signal, and the resulting electrical signal is processed to reconstruct OCT images. To acquire the reflected spectrum from the grating for temperature data extraction, an optical spectrum analyzer (AQ6370C, YOKOGAWA) is integrated before the photodetector. Specifically, a 90/10 coupler is inserted downstream of the first 50/50 coupler to allocate 10% of the light source to the FBG interrogator, while an optical fiber attenuator is used on the other side to ensure that the signal strengths entering the detector are consistent. To ensure equal optical path lengths before the detector, it is essential to connect a fiber optic patch cable—with a length matching that of the 90/10 coupler—to the optical path without the 90/10 coupler.

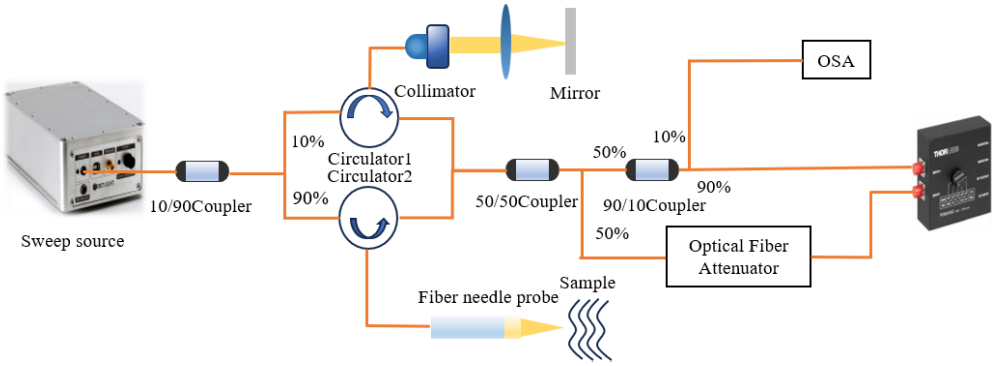

Fig. 4. Schematic Diagram of OCT-FBG System (OSA: Optical Spectrum Analyzer; all interconnections between components are single-mode optical fibers)

In this system, the spectral modifications introduced by the FBG—both the reflected component returning to the system and the notched spectrum probing the sample—influence the OCT imaging. The spectral dip at the Bragg wavelength in the transmission spectrum causes a reduction in intensity or loss of signal from specific depths, although this information loss is negligible. At the same time, it also elevates the side lobes flanking the A-scan peak, leading to a slight degradation in image contrast. This is also acceptable. The most significant impact, however, stems from the reflection spectrum, which introduces common noise and artifacts that substantially compromise the quality of the OCT image. Therefore, critical constraints on grating performance are essential to mitigate these adverse effects.

3.2. Experimental preparation

To investigate the impact of gratings on OCT imaging, fiber probes with gratings of varying parameters were fabricated for imaging experiments. The Bragg wavelength and the grating reflectance are two key parameters that can potentially affect OCT imaging quality. And the Bragg wavelength determines the relative position of its reflected spectrum with respect to the OCT light source's spectrum. Reflectivity determines the balance between the strength of the returned sensor signal and the degradation of OCT image quality. This degradation primarily stems from the spectral dip formed by the FBG within the OCT light source spectrum, which may generate sidelobe artifacts and increase noise in reconstructed OCT images. Therefore, we prepared a total of 9 fiber probes inscribed with gratings of varying grating lengths, refractive

Optics EXPRESS

index modulation depths, and Bragg wavelengths (other parameters are consistent). The refractive index modulation depth was controlled by adjusting the laser writing power, and the specific parameters of the Bragg gratings are listed in Table 1. First, Bragg wavelengths of 1310 nm and 1350 nm (with actual fabricated values of 1306 ± 0.2 nm and 1346 ± 0.2 nm, respectively) were selected to represent positions near the center and the edge of the broadband OCT source spectrum, allowing us to evaluate the effect of the grating's spectral location on imaging. Second, the grating length and the laser writing power were varied as the primary means to achieve a range of grating reflectivity (from high to low), to investigate the effect of grating reflectance on OCT imaging, wherein the grating length was carefully moderated to avoid excessive length that would compromise point-temperature measurement capability, while preventing excessively short lengths that could induce spectral distortion; simultaneously, the selected laser power was maintained within the tolerable range of the fiber and optimized for effective grating fabrication.

In Table 1, the grating length and inscription laser power are the preset parameters controlled by the fabrication software during the femtosecond laser writing process. The Bragg wavelength and reflectance are the as-fabricated optical properties of each probe. The reflected spectrum and transmitted spectrum of the grating were measured with an optical spectrum analyzer (AQ6370C, YOKOGAWA) to evaluate its performance. The reflectance of a grating can be derived from its transmittance spectrum to minimize the impact of the system's baseline noise. The wavelength shift of a fiber Bragg grating's reflectance spectrum is used for temperature measurement. The Bragg wavelength and reflectance values of the grating are the average of three measurements.

3.3. Imaging experiments

To evaluate the feasibility of imaging fiber-optic probes with gratings, the effect of FBGs with varying characteristics on OCT images must be investigated. A high-precision motorized linear stage (CXPF100-80157) was used to perform a linear scan with the fiber probe for imaging the adhesive tape.

The reflectivity of a Bragg grating is closely associated with its grating length and refractive index modulation depth: a longer grating or larger refractive index modulation depth leads to higher reflectivity, which in turn results in more light being reflected. In this OCT-FBG system, the center wavelength of the FBG probe must match the operating wavelength band of the OCT. So, the FBG introduces noise during the imaging process. To ensure system performance, the FBG reflectance must be controlled within an appropriate range. On the one hand, the reflected spectral signal must be sufficiently detectable to enable reliable temperature monitoring. On the other hand, the reflected light intensity must not be excessively high. Excessively high reflectance would cause the reflected spectral signal to overwhelm the OCT imaging signal. Furthermore, an extreme amount of light being reflected also means excessive attenuation in the transmission spectrum, which could lead to the loss of partial sample information, potentially degrading the OCT image quality or causing a loss of effective structural information. Therefore, the reflected light intensity must not be so high as to interfere with the OCT image signal.

Figure 5(a) shows the tape M-scans corresponding to fiber probes with different grating lengths or laser powers at a Bragg wavelength of 1306 and 1346 nm. When the grating reflectance is high (probe 1-3), it causes significant interference in OCT imaging: higher reflectance results in stronger reflected light signals, which mask the OCT imaging signals and introduce extensive artifacts in the images. As the grating length decreases or the writing laser power is reduced (corresponding to a decrease in refractive index modulation depth), the artifacts in the OCT image gradually diminish, ultimately enabling effective OCT imaging (probe 4-8). Experimental results indicate that to keep the FBG's impact on OCT images within an acceptable range, the grating reflectivity should be maintained at 24% or below. Figure 5(b) presents the B-scans obtained using a fiber grating probe 4-8 and a non-grating probe 9. The reflectance of all gratings used was maintained at 24% or below, and the B-scans reveal the layered structure of the tape.

Optics EXPRESS

As the grating reflectance decreases, the OCT image quality improves significantly, progressively approaching the results achieved with a grating-free fiber probe, with the individual tape layers becoming increasingly distinct. Between probes 4 and 5, which both have a reflectance of 24%, probe 5 (Bragg wavelength: 1346 nm) produces clearer OCT images. The key point is that the OCT light source used in this experiment exhibits a spectral intensity distribution that is essentially Gaussian, with peak intensity near 1306 nm. Experimental verification confirms that when the FBG's Bragg wavelength is 1306 nm, and its reflectance is 24% or lower, the OCT imaging quality is acceptable. This reflectance threshold also applies to a 1346 nm grating whose Bragg wavelength lies on the side of the light source spectrum with lower spectral intensity; moreover, at the same reflectance level, the latter grating yields superior imaging performance. Therefore, this reflectance threshold is broadly applicable within the spectral range where peak intensity is below 1306 nm in the light source spectrum. For spectral regions with intensity exceeding the 1306 nm peak, appropriately reducing the grating's reflectivity may be considered to ensure imaging quality. In other words, as long as the grating's reflectivity is controlled at sufficiently low levels to support imaging, the Bragg wavelength can be freely selected within the usable spectral range of the OCT light source. Experiments demonstrate that when selecting a Bragg wavelength within the spectral bandwidth of the OCT light source for temperature sensing, using a low-reflectivity weak grating can reduce its interference with OCT imaging to an acceptable level. This fully validates the feasibility of simultaneously achieving temperature sensing and structural imaging via an OCT-FBG fiber probe, using a single OCT light source without the need for an external light source.

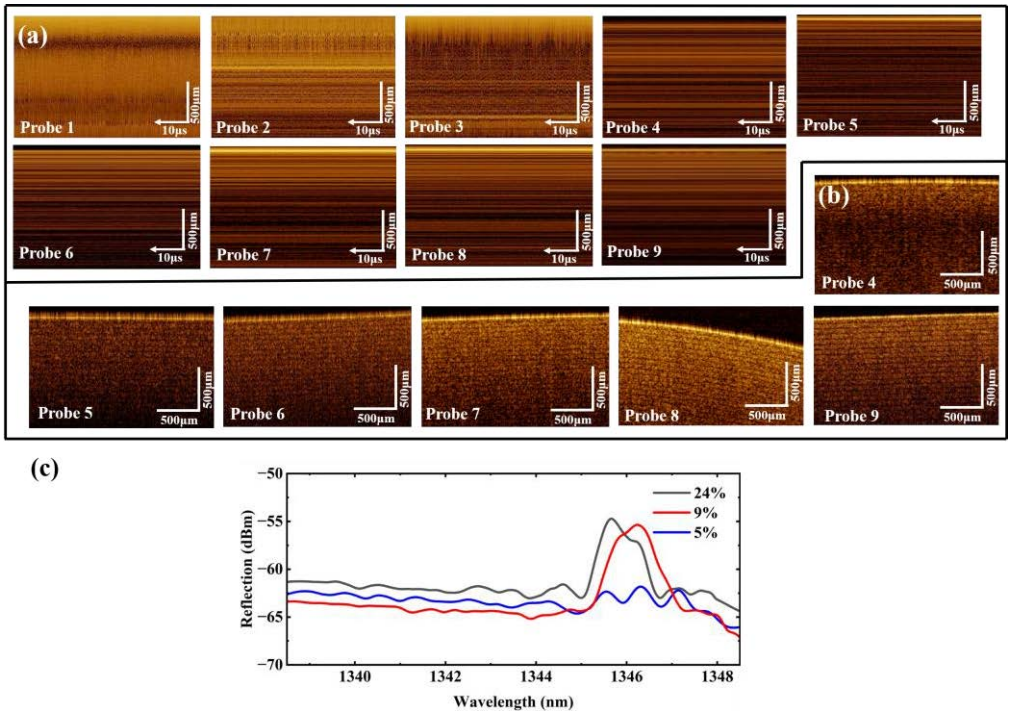

Fig. 5. OCT images of adhesive tape using fiber probes with different gratings. M-scan: It is generated by repeatedly acquiring A-scans from a single, fixed point on the sample at high temporal frequency; B-scan: It is constructed by acquiring a series of consecutive A-scans (Axial scans) while the OCT beam is laterally scanned across the sample along a single axis. (a) M-scans formed by probes 1-9. (b) B-scans formed by probes 4-9. (c) Reflectance spectra from probes 5(24%), 6(9%), and 7(5%) in the system.

Optics EXPRESS

It is noteworthy that although lower grating reflectivity typically enhances OCT imaging performance, the spectrometer employed in this system is limited by its detection threshold for weak signals. As illustrated in Fig. 5(c), the spectrometer enables reliable signal detection when the grating reflectivity is 9%. When the reflectivity is reduced to 5%, however, the detected grating reflection spectrum becomes distorted, rendering it unreliable for reference.

3.4. Temperature sensitivity experiment

Since this OCT-FBG integrated system employs a fiber optic spectrometer to measure reflected spectral signals, the low reflectivity of the grating resulted in reflected spectral signals that were too weak to be detected. Meanwhile, according to the theoretical formula (5) for FBGs, gratings with larger Bragg wavelengths exhibit higher temperature sensitivity. Thus, probe 5(1.25 mm/18%/1345.9 nm, reflectance 24%) was ultimately selected for experiments. As shown in Fig. 6(a), the temperature sensitivity of this probe was measured using a water bath: a heating plate was used to warm the water in a beaker, with the grating section of the probe submerged in the water; a fiber optic spectrometer measured the grating's reflected wavelength, while a resistance thermometer measured the water temperature as a reference. During the temperature rise process, the grating reflection spectrum shifts to the right (Fig. 6(b)). Figure 6(c) presents the relationship curve between the grating reflection wavelength and temperature. The temperature sensitivity of this probe was 10.14 pm/°C.

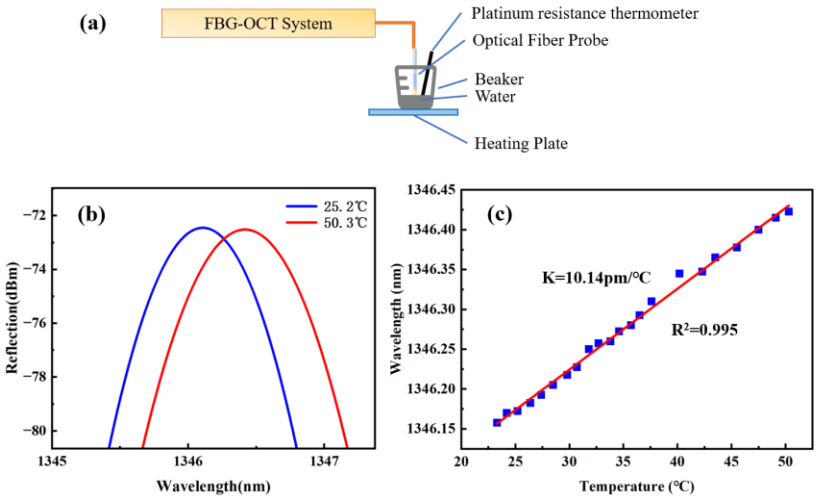

Fig. 6. (a) Experimental setup for FBG temperature sensing. (b) Reflectance spectrum shifts rightward with increasing temperature. (c) Relationship between reflected wavelength and temperature during temperature elevation: the curve slope, representing temperature sensitivity, is 10.14 pm/°C, with $R^2 = 0.995$

3.5. Simultaneous imaging and temperature sensing experiments on in vitro tissue

To validate the probe's feasibility, OCT imaging and temperature measurements within the biologically relevant temperature range were conducted on the mouse brain and porcine backfat using this probe and the OCT-FBG integrated system. The probe tip was inserted into the mouse brain; analogous to the previous experiment, a water bath method was employed to alter the brain temperature. Temperature changes during heating and cooling processes were recorded concurrently with brain imaging. To prevent the grating from being affected by insertion stress, the probe can be retracted slightly after insertion. Before inserting the probe into the mouse

Optics EXPRESS

brain, a high-precision motorized linear stage controls the translation of the fiber probe for mouse brain coronal plane imaging, providing more comprehensive validation of the probe's imaging capabilities.

Figure 7(a) shows the temperature change curves of a mouse brain during heating and cooling to room temperature, alongside the water temperature curve measured by a resistance thermometer. The trends of the two curves are consistent. Due to the small size of the mouse brain, the temperatures of the two curves are essentially identical. Figure 7(c) corresponds to M-mode imaging during the temperature measurement process, confirming the feasibility of simultaneous temperature measurement and imaging. Before the water bath experiment, two-dimensional OCT imaging of the mouse brain in the coronal plane was carried out using a high-precision motorized linear stage (Fig. 7(b)) to evaluate the imaging performance of the probe further. This needle probe can be inserted into tissue to obtain information about deep structures. Figure 7(d) shows an M-mode image acquired during the insertion and withdrawal of the probe into the mouse brain, revealing distinct structural layers including the cerebral cortex, corpus callosum, septum pellucidum, and fornix, which have clearly defined boundaries.

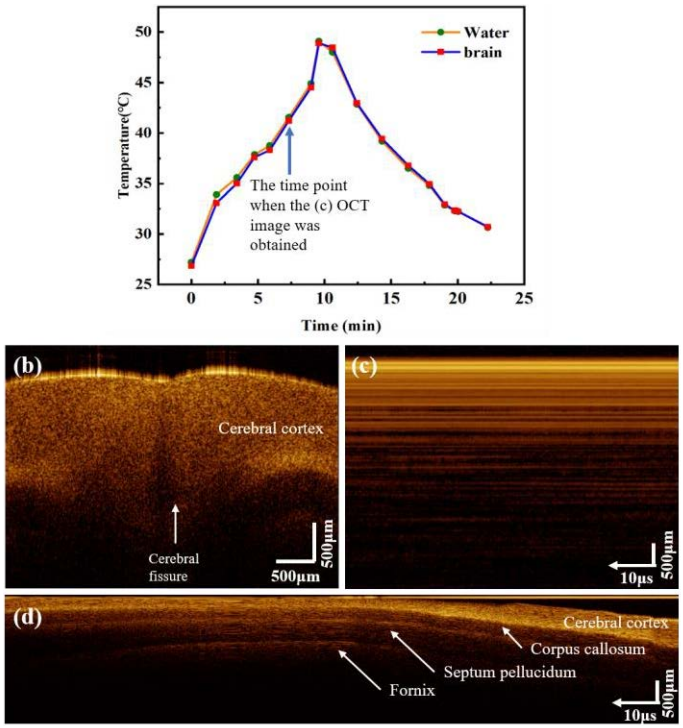

Fig. 7. (a) Curve of mouse brain temperature change measured by the probe during the experiment and curve of water temperature change measured by the resistance thermometer; (b) B-scan of a specific coronal plane of the brain; (c) M-scan at a specific moment during temperature measurement after the probe was inserted into the rat brain; (d) M-mode structural OCT image during probe insertion and withdrawal from the brain (recording the A-scan from right to left during the insertion and withdrawal process).

To validate the probe's capability for real-time dual-mode monitoring of heat-induced structural changes, this experiment employed porcine dorsal fat as a mature tissue model. The experiment simulated scenarios such as fat-targeted thermotherapy. The backfat was cut into appropriately sized cubes. Heating was applied beneath the tissue via a glass slide, while the probe remained stationary within the tissue for imaging and temperature measurement. As shown in Fig. 8,

Optics EXPRESS

during heating, the fat crystals in the tissue underwent a phase transition, gradually melting from a solid to a liquid state. This structural change resulted in significant alterations in the brightness and texture features of the OCT images. Overall, the total scattering signal in the OCT images exhibited a decreasing trend as the temperature increased. This phenomenon was primarily attributed to the melting of solid-phase fat crystals, which substantially reduced the number of light-scattering interfaces in the sample (Fig. 8(a) - (l)). The melted fat formed an optically homogeneous liquid medium, appearing as low-scattering dark regions in the OCT images (Fig. 8(i), (j), (k)), and the extent of these dark regions progressively expands during heating. Due to the lower scattering efficiency of liquid fat, the penetration capability of incident light increases, thereby enhancing detection depth. This change is evident in the images as a transient increase in signal intensity in deeper regions (Fig. 8(e)-(h)), which subsequently decays to background levels as the scattering particles are eliminated. Ultimately, the OCT image evolves from its initial bright morphology with high scattering properties (Fig. 8(a)) into a characteristic pattern featuring interwoven bright (solid structures) and dark (liquid fat) regions, exhibiting an overall reduction in scattering intensity (Fig. 8(l)).

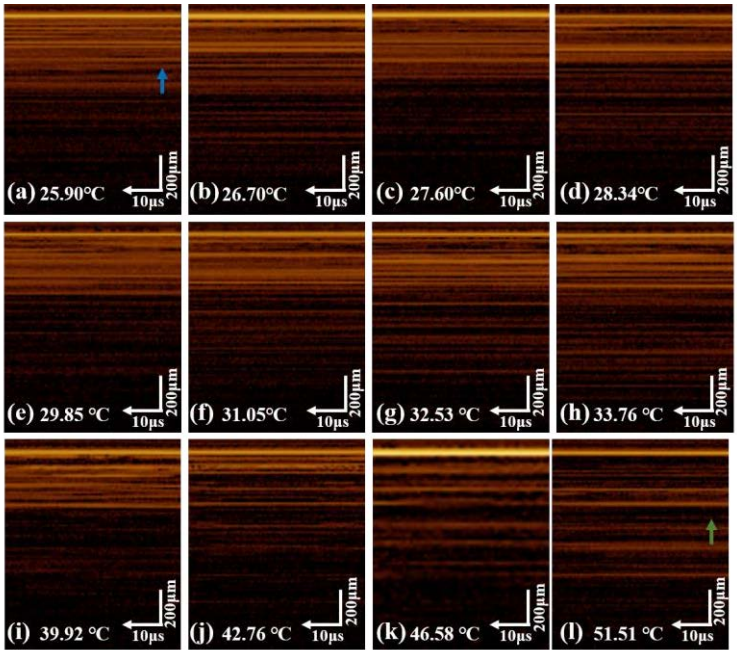

Fig. 8. M-scan images during heating and corresponding temperatures. The OCT image series (a)-(l) shows the dynamic evolution of the microstructure of porcine backfat tissue during heating from 25.90°C (a) to 51.51°C (l). With increasing temperature, the tissue transitions from an initial state of uniform, high signal scattering (for example, the section indicated by the blue arrow) to the gradual emergence of localized no-signal areas (green arrow). This progression indicates lipid melting and the loss of scattering interfaces.

Figure 9(a) shows a steady rise from 17.49°C to 51.51°C. Figure 9(b) and (c) show OCT B-scans obtained using an electric displacement stage, with tissue temperature measured by a resistance thermometer. The B-scan acquired at the lower temperature prior to heating (b, ~16°C) contrasts sharply with that obtained at the higher temperature post-heating (c, ~28°C): optical scattering in adipose tissue is reduced, with images appearing noticeably darker and structural contrast diminished. This phenomenon is fully consistent with the previously analyzed

Optics EXPRESS

mechanism: the melting of lipid crystals causes a significant decrease in the tissue's optical scattering coefficient, leading to signal attenuation.

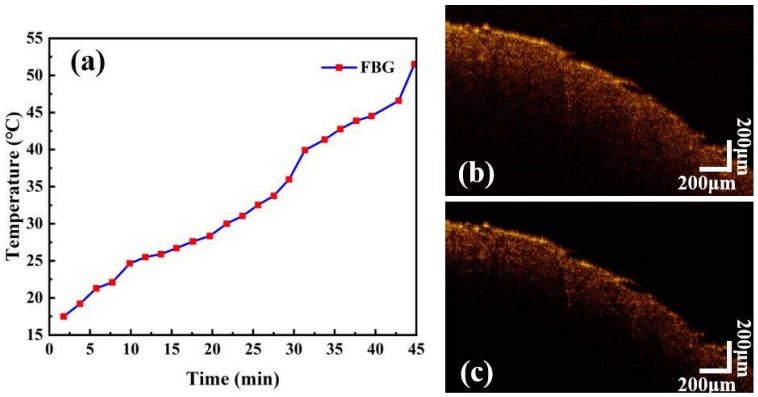

Fig. 9. (a) Temperature change curve of pig backfat measured by FBG during the experiment. (b) B-scan of backfat before heating, corresponding to a temperature of ~ 16 ℃. (c) B-scan of heated pork back fat, corresponding to a temperature of ~ 28℃.

4. Conclusions

In summary, we have developed a miniaturized dual-modal fiber-optic probe that integrates OCT imaging and FBG temperature sensing. The miniaturized probe with an outer diameter of 0.51 mm and a lateral resolution of ~30 μm simultaneously achieves OCT imaging with a tissue penetration depth of 1–1.5 mm and temperature measurement with a sensitivity of 10.14 pm/℃. Crucially, it was experimentally verified for the first time that the FBG's Bragg wavelength can be positioned within the OCT source band, a fundamental requirement for a shared light source. Through the fabrication and testing of FBGs with varied parameters, it was found that a low reflectivity ($\leq 24\%$) was necessary to avoid significant image artifacts. The probe's functionality within biological tissues was confirmed by performing real-time, simultaneous temperature measurement and OCT imaging during its insertion into the mouse brain and porcine backfat. The current forward-viewing design is limited to M-scans during penetration; a future side-viewing configuration is proposed to enable B-scan or radial scanning for comprehensive imaging.

Funding. National Natural Science Foundation of China (62475161, T2421003).

Acknowledgment. The author acknowledges the support and assistance provided by the University of Shanghai for Science and Technology, Shenzhen University, and the Xi'an Institute of Optics and Precision Mechanics for this research.

Disclosures. The authors declare no conflicts of interest.

Data availability. Data underlying the results presented in this paper are not publicly available at this time but may be obtained from the authors upon reasonable request.

References

1. K. Nishimiya and G. Tearney, "Multimodality intravascular optical coherence tomography," Curr. Opin. Biomed. Eng. **9**, 57–65 (2019).
2. K. Nishimiya and G. Tearney, "Micro optical coherence tomography for coronary imaging," Front. Cardiovasc. Med. **8**, 613400 (2021).
3. A. M. Fard, P. Vacas-Jacques, E. Hamidi, *et al.*, "Optical coherence tomography – near infrared spectroscopy system and catheter for intravascular imaging," Opt. Express **21**(25), 30849 (2013).
4. J. Wang, K. Tao, W. Zhu, *et al.*, "A FBG-OCT catheter to reconstruct vascular shape in intravascular optical coherence tomography," IEEE Photonics Technol. Lett. **31**(9), 701–704 (2019).

Optics EXPRESS

5. N. R. Holm, L. N. Andreasen, O. Neghabat, *et al.*, "OCT or angiography guidance for pci in complex bifurcation lesions," N. Engl. J. Med. **389**(16), 1477–1487 (2023).
6. R. Kong, C. Dai, Q. Zhang, *et al.*, "Integrated US-OCT-NIRF tri-modality endoscopic imaging system for pancreaticobiliary duct imaging," IEEE Trans. Ultrason., Ferroelect., Freq. Contr. **69**(6), 1970–1979 (2022).
7. W. Yuan, R. Brown, W. Mitzner, *et al.*, "Super-achromatic monolithic microprobe for ultrahigh-resolution endoscopic optical coherence tomography at 800 nm," Nat. Commun. **8**(1), 1531 (2017).
8. B. Tan, Z. Hosseinaee, L. Han, *et al.*, "250 kHz, 15 µm resolution SD-OCT for in-vivo cellular imaging of the human cornea," Biomed. Opt. Express **9**(12), 6569 (2018).
9. J. Xi, A. Zhang, Z. Liu, *et al.*, "Diffractive catheter for ultrahigh-resolution spectral-domain volumetric OCT imaging," Opt. Lett. **39**(7), 2016 (2014).
10. A. D. Aguirre, P. R. Herz, Y. Chen, *et al.*, "Two-axis MEMS scanning catheter for ultrahigh resolution three-dimensional and en face imaging," Opt. Express **15**(5), 2445–2453 (2007).
11. J. Kim, J. Xing, H. S. Nam, *et al.*, "Endoscopic micro-optical coherence tomography with extended depth of focus using a binary phase spatial filter," Opt. Lett. **42**(3), 379 (2017).
12. B. Yin, K. K. Chu, C.-P. Liang, *et al.*, "µOCT imaging using depth of focus extension by self-imaging wavefront division in a common-path fiber optic probe," Opt. Express **24**(5), 5555 (2016).
13. G. K. Krasin, M. A. Vinogradov, M. S. Kovalev, *et al.*, "Investigation of parameters of the Bessel beam formed by an axicon," in *Optical Sensors 2019*, (2019).
14. K. Beaudette, J. Li, J. Lamarre, *et al.*, "Double-clad fiber-based multifunctional biosensors and multimodal bioimaging systems: technology and applications," Biosensors **12**(2), 90 (2022).
15. K. Beaudette, N. Godbout, and C. Boudoux, "Advances in multimodal imaging using double-clad fiber couplers," J. Lightwave Technol. **37**(22), 5674–5685 (2019).
16. S. Liang, A. Saidi, J. Jing, *et al.*, "Intravascular atherosclerotic imaging with combined fluorescence and optical coherence tomography probe based on a double-clad fiber combiner," J. Biomed. Opt. **17**(7), 0705011 (2012).
17. Y. Chen, "Recent advances in fluorescent probes for extracellular pH detection and imaging," Anal. Biochem. **612**, 113900 (2021).
18. J. Qiao, C. Chen, D. Shangguan, *et al.*, "Simultaneous monitoring of mitochondrial temperature and ATP fluctuation using fluorescent probes in living cells," Anal. Chem. **90**(21), 12553–12558 (2018).
19. P. K. Capon, J. Li, A. J. Horsfall, *et al.*, "A silk-based functionalization architecture for single fiber imaging and sensing," Adv. Funct. Mater. **32**(3), 2010713 (2022).
20. E. P. Schartner, M. R. Henderson, M. Purdey, *et al.*, "Cancer detection in human tissue samples using a fiber-tip pH probe," Cancer Res. **76**(23), 6795–6801 (2016).
21. J. Li, E. Schartner, S. Musolino, *et al.*, "Miniaturized single-fiber-based needle probe for combined imaging and sensing in deep tissue," Opt. Lett. **43**(8), 1682 (2018).
22. M. Yu, F. Li, Z. Chen, *et al.*, "Laser scanning up-conversion luminescence microscopy for imaging cells labeled with rare-earth nanophosphors," Anal. Chem. **81**(3), 930–935 (2009).
23. A. Tanskanen, G. Hohert, A. Lee, *et al.*, "Higher-order core-like modes in double-clad fiber contribute to multipath artifacts in optical coherence tomography," J. Lightwave Technol. **39**(17), 5573–5581 (2021).
24. B. A. Tahir, J. Ali, and R. A. Rahman, "Fiber Bragg grating based system for temperature measurements," Int. J. Mod. Phys. B **23**(10), 2349–2356 (2009).
25. U. M. Pal, A. Vishnu Gk, M. Varma, *et al.*, "Thermo-optic measurements and their inter-dependencies for delineating cancerous breast biopsy tissue from adjacent normal," J. Biophotonics **14**(8), 202100041 (2021).
26. J. Kang, R. Zhu, Y. Sun, *et al.*, "Pencil-beam scanning catheter for intracoronary optical coherence tomography," Opto-Electron. Adv. **5**(3), 200050 (2022).
27. C. Jin, X. Tong, C. Zhang, *et al.*, "Study on the structure and optical imaging characteristics of an all-fiber OCT probe," Opt. Eng. **59**(08), 085101 (2020).
28. P. Cheng, L. Wang, Y. Pan, *et al.*, "Fiber Bragg grating temperature sensor of cladding with SrTiO3thin film by pulsed laser deposition," Laser Phys. **29**(2), 025107 (2019).
29. I. Dhingra, G. Kaur, and R. S. Kaler, "Design and analysis of fiber Bragg grating sensor to monitor strain and temperature for structural health monitoring," Opt. Quantum Electron. **53**(11), 619 (2021).